References

BLAUROCK, A. E. & WORTHINGTON, C. R. (1964). *Biophys. J.* **6**, 305.

BLODGETT, K. B. (1935). *J. Amer. Chem. Soc.* **57**, 1007.

HOSEMANN, R. & BAGCHI, S. N. (1962). *Direct Analysis of Diffraction by Matter*, pp. 122–131. Amsterdam: North Holland.

LESSLAUER, W. & BLASIE, J. K. (1971). *Biophys. J.* In the press.

LUZZATI, V. (1968). In *Biological Membranes*, pp. 71–123. Edited by D. CHAPMAN. London: Academic Press.

LEVINE, Y. K., BAILEY, A. I. & WILKINS, M. H. F. (1968). *Nature, Lond.* **220**, 577.

SMITH, H. M. (1969). *Principles of Holography*, p. 19. New York: John Wiley.

WINTHROP, J. T. & WORTHINGTON, C. R. (1965). *Phys. Letters*, **15**, 124.

Acta Cryst. (1971). A**27**, 461

The Resolution Function of a Slow Neutron Rotating Crystal Time-of-Flight Spectrometer I. Application to Phonon Measurements

BY A. FURRER

Delegation für Ausbildung und Hochschulforschung am Eidg. Institut für Reaktorforschung, Wuerenlingen, Switzerland

(*Received* 6 *October* 1970)

The resolution function of a slow neutron rotating crystal time-of-flight spectrometer applied to phonon measurements is treated analytically. It is demonstrated that every component of the instrument may contribute to the uncertainty of the time-of-flight measurement. Focusing conditions are derived leading to the concept of removable and irremovable time-of-flight spreads. No approximations are made concerning the phonon dispersion surface. Experimental evidence is presented to support the resolution functions calculated on the basis of this theory.

1. Introduction

In the course of the past decade the scattering of thermal neutrons has proved to be one of the most versatile experimental techniques for studying dynamics and structure of solids and liquids. Fig. 1 shows a schematic sketch of a slow neutron spectrometer. The essential parts are the neutron source, the monochromator system, the sample, and the analyser system, elements of which are denoted by the indices 0, 1, 2, 3 according to the order in which they are located along the neutron flight-path. Intermediate elements such as collimators C, flight-paths L, and neutron wave-vectors $\mathbf{k}$ have double indices. The experimental spectrum $I(\mathbf{Q},\omega)$ observed by the analyzer is given by the convolution integral

$$I(\mathbf{Q},\omega)=\iint R(\mathbf{Q}'-\mathbf{Q},\omega'-\omega)\sigma(\mathbf{Q}',\omega')\mathrm{d}\mathbf{Q}'\mathrm{d}\omega' , \quad (1{\cdot}1)$$

where $R(\mathbf{Q},\omega)$ is the instrumental resolution function and $\sigma(\mathbf{Q},\omega)$ is the unknown scattering cross section. The variables $\mathbf{Q},\omega$ are defined by the momentum transfer

$$\hbar\mathbf{Q}=\hbar(\mathbf{k}_{12}-\mathbf{k}_{23}) \quad (1{\cdot}2)$$

and by the energy transfer

$$\hbar\omega=\frac{\hbar^2}{2m}(k_{12}^2-k_{23}^2) , \quad (1{\cdot}3)$$

where m denotes the neutron mass. The problem is to evaluate $\sigma(\mathbf{Q},\omega)$ by an unfolding procedure, provided $R(\mathbf{Q},\omega)$ is known. The most accurate method of determining $R(\mathbf{Q},\omega)$ would be a direct measurement requiring no prior knowledge of instrumental parameters. This, however, is usually impossible except for zero energy transfer, so that in general $R(\mathbf{Q},\omega)$ will have to be calculated. This was done analytically by Collins (1963), Peckham, Saunderson & Sharp (1967),

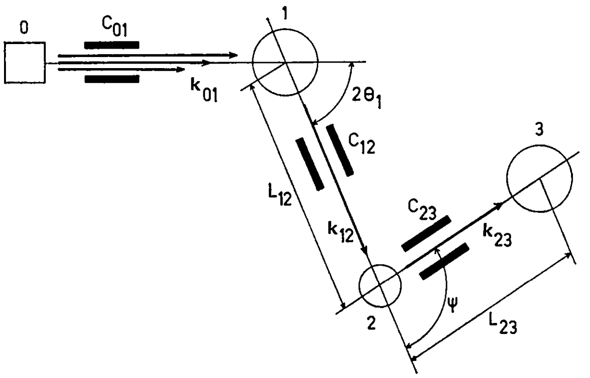

Fig. 1. Schematic sketch of a slow neutron spectrometer. 0: neutron source, 1: monochromator system, 2: sample, 3: analyser system.

Cooper & Nathans (1967), Stedman (1968), and Nielsen & Bjerrum Møller (1969) for a triple-axis spectrometer and Komura & Cooper (1970) for a twin-rotor time-of-flight spectrometer.

The present paper contains an analytical treatment of the resolution function of a rotating crystal time-of-flight spectrometer applied to the measurement of phonon dispersions $\omega(\mathbf{q})$, where $\mathbf{q}$ is the phonon wave vector. This goes considerably beyond Brockhouse (1961), Carvalho, Ehret & Gläser (1967), and others, who restricted their investigations to some general instrumental features. It is shown that every component of the spectrometer contributes to the uncertainty of the time-of-flight measurement. The corresponding time-of-flight spreads are calculated quantitatively. Furthermore, with a view towards developing an optimum focusing procedure it is investigated which of the uncertainties can be reduced or even eliminated. Hence, uncertainties in the time-of-flight measurement will be separated into two groups which will be called the *removable* and the *irremovable* time-of-flight uncertainties. The assumption is made that the variation of the flight-paths L due to the vertical dimension of the monochromator, of the sample, and of the detector is ignored. However, this approximation has only a negligible influence on the instrumental resolution function, because the flight-paths of a time-of-flight spectrometer are very much longer than the vertical dimensions mentioned above.

The dependence of the resolution function upon geometrical factors such as the shape of the monochromator, of the sample, and of the detector is a characteristic of time-of-flight spectrometers. In order to take account of these geometry effects it is useful to pursue the neutron flight-paths in real space and to describe the instrumental resolution as a function of the neutron flight-time T given by

$$T=\frac{mL_{12}}{\hbar k_{12}}+\frac{mL_{23}}{\hbar k_{23}}+\Delta T\,. \qquad (1\cdot4)$$

ΔT includes terms arising from geometrical factors as well as from the time delay of the incident neutrons. k_{23} follows from the phonon scattering surface which is defined as the locus of end-points of vectors $\mathbf{Q}$ and $-\mathbf{k}_{23}$ satisfying equations (1·2) and (1·3), provided $\mathbf{k}_{12}$ is fixed relative to the crystal lattice. This means that the flight-time T depends on the phonon scattering law $\sigma(\mathbf{Q},\omega)$. Therefore it is useful to introduce an effective resolution function for phonon scattering defined as the probability for detecting neutrons in the time interval dT when the spectrometer has been set to yield the phonon $\omega(\mathbf{q})$ resulting from the scattering process:

$$R_\sigma(T)=\iint g_{12}(\mathbf{k}_{12})R(\mathbf{k}_{12}-\mathbf{k}_{23},T)\mathrm{d}\mathbf{k}_{12}\mathrm{d}\mathbf{k}_{23}\,. \qquad (1\cdot5)$$

$R(\mathbf{k}_{12}-\mathbf{k}_{23},T)$ is equal to $R(\mathbf{Q},T)$ and denotes the conventional resolution function defined by equation (1·1) in the time-of-flight scale. $g_{12}(\mathbf{k}_{12})$ is the probability function for the incident neutrons. The integration over $\mathbf{k}_{23}$ is limited to the phonon scattering surface which is considered to have zero energy width. The index σ points to the dependence on the scattering surface. Under the assumption that the change of the resolution function is negligibly small over the frequency range dω given by the finite width of the dispersion surface, while $\mathbf{Q}$ is kept constant, equation (1·1) then becomes

$$I(T)=\int R_\sigma(T'-T)\sigma(T')\mathrm{d}T'\,, \qquad (1\cdot6)$$

where $\sigma(T)$ is the line shape of the phonon with wave-vector $\mathbf{Q}$. In order to derive the unknown function $\sigma(T)$ from the measured time-of-flight spectrum, equation (1·6) suggests that it would be preferable to determine directly the effective resolution function for phonon scattering $R_\sigma(T)$ rather than to calculate first the instrumental resolution function $R(\mathbf{Q},T)$.

The removable time-of-flight uncertainties are described in §2. Focusing conditions are given to reduce the time-of-flight spreads arising from the wave-number distribution g_{12} of the incident neutrons and from the Doppler effect. There follow in §3 the irremovable contributions to $R_\sigma(T)$ resulting from the mosaic

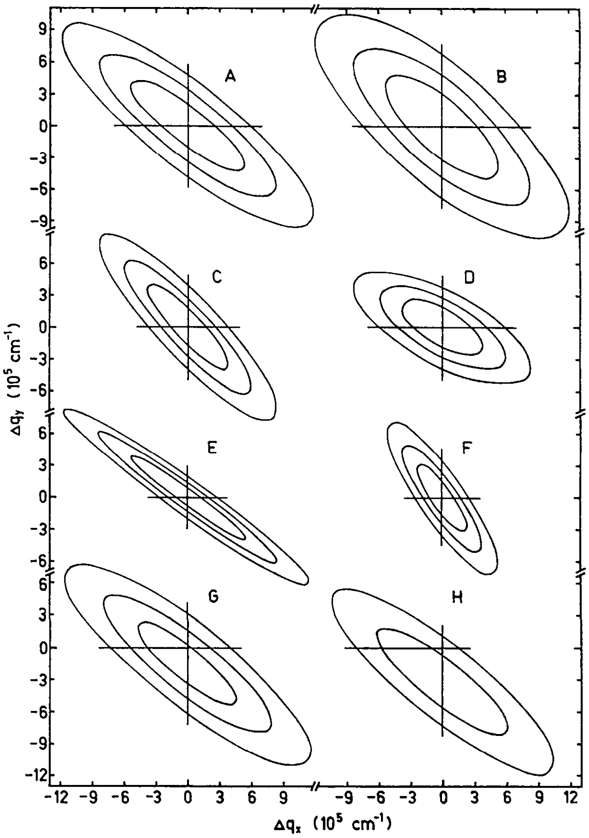

Fig. 2. Wave-number distribution of neutrons scattered by the monochromator in a horizontal plane for several sets of instrumental parameters. The appropriate values of g_{12} are 0·75, 0·50 and 0·25 respectively, for the inner, middle and outer ellipses.

spreads ξ_2 and η_2 of the sample, of the collimations α_{23} and β_{23}, of the sample thickness, and of the detector thickness. To illustrate and support the preceding considerations §4 presents a series of experimental results. Some final conclusions are given in §5.

2. Removable time-of-flight uncertainties

2·1 *Monochromator ellipsoid*

Whenever the condition of Bragg's law

$$n\lambda = 2d \sin\theta_1 \quad (n=1, 2, 3, \ldots) \tag{2·1}$$

is fulfilled by the reflecting planes of the rotating monochromator whose interplanar distance is given by d, neutrons of wavelength λ (wavelengths of order higher than $n=1$ can often be suppressed by filters) are scattered into the direction determined by the angle $2\theta_1$. Assuming Gaussian transmission functions of Soller collimators and Gaussian mosaic spreads of single crystals, the wave-number distribution of the emitted neutrons is given by

$$\begin{aligned} g_{12}(k'_{12},\gamma_{12},\delta_{12},t) &= g_0(k'_{12})p_1(k'_{12})\frac{1}{2a}\sqrt{\frac{\pi}{\ln 2}} \\ &\times \exp\left\{-\frac{4\ln2}{\alpha_{01}^2}\left[\gamma_{12}-2\left(1-\frac{k'_{12}}{k_{12}}\right)\operatorname{tg}\theta_1\right]^2\right. \\ &-\frac{4\ln2}{\xi_1^2}\left[\gamma_{12}-\left(1-\frac{k'_{12}}{k_{12}}\right)\operatorname{tg}\theta_1-2\pi\left(vt-\frac{u}{w}\right)\right]^2 \\ &\left.-\frac{4\ln2}{\alpha_{12}^2}\gamma_{12}^2-\frac{4\ln2}{\beta_{01}^2+4\eta_1^2\sin^2\theta_1}\delta_{12}^2-\frac{4\ln2}{\beta_{12}^2}\delta_{12}^2\right\} \end{aligned} \tag{2·2a}$$

with

$$a=\sqrt{\frac{1}{\beta_{01}^2}+\frac{1}{4\eta_1^2\sin^2\theta_1}}\ , \tag{2·2b}$$

which is derived in Appendix *A*. γ_{12} and δ_{12} are the horizontal and vertical divergence angles with respect to the optimum emission direction, α and β the horizontal and vertical half-widths of the transmission function of the collimators, ξ and η the half-widths of the mosaic spread in the horizontal and vertical plane respectively, g_0 is the wave-number distribution of the neutrons emitted from the source, p_1 the monochromator reflectivity, k_{12} the mean wave-number $\frac{\pi}{d\sin\theta_1}$ derived from equation (2·1), v the spin velocity of the rotating crystal, w the number of reflecting planes of the monochromator, and u an integer index denoting the number of neutron bursts already emitted at the time t. The form of g_{12} is nearly ellipsoidal and will be called the *monochromator ellipsoid*. It is illustrated in Fig. 2 for several sets of instrumental parameters given in Table 1. Since in a first approximation the wave-number and the direction of the neutron beam are correlated only with respect to its horizontal divergence, Fig. 2 shows cross sections through the monochromator ellipsoid in a horizontal plane. Focusing effects become possible due to the asymmetric shape of the wave-number distribution relative to the mean emission direction.

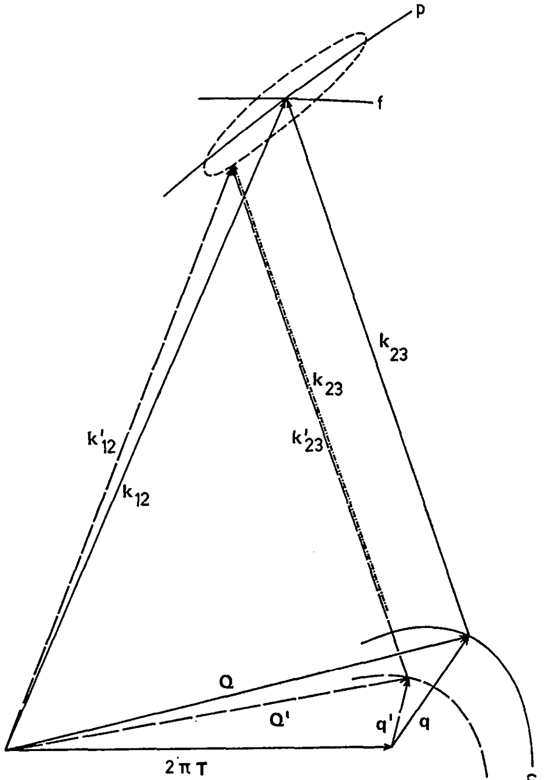

Fig. 3. Schematic representation of the neutron scattering process by phonons in reciprocal space. The dotted line symbolizes the monochromator ellipsoid whose principal axis and focusing surface are denoted by p and f respectively. The phonon scattering surface is given by S.

Table 1. *Instrumental parameters used to calculate the monochromator ellipsoid shown in Fig.* 2

	α_{01}	ξ_1	α_{12}	θ_1	K_{12}[Å^{-1}]	t[μsec]	ν[sec^{-1}]
A	30′	15′	30′	35°	1·92	0	200
B	30	30	30	35	1·92	0	200
C	15	15	30	35	1·92	0	200
D	30	15	15	35	1·92	0	200
E	30	5	30	35	1·92	0	200
F	30	15	30	50	1·44	0	200
G	30	15	30	35	1·92	1	200
H	30	15	30	35	1·92	2	200

Fig. 3 gives a schematic sketch of the scattering process in reciprocal space for two pairs of neutron wavevectors belonging respectively to the centre and to any point of the monochromator ellipsoid. The direction of the scattered neutrons is kept constant; its variation within the angular limits determined by the collimator C_{23} contributes to the irremovable time-of-flight uncertainty as will be discussed in the following section. The resulting phonon frequencies ω,ω' and wave-vectors $\mathbf{q},\mathbf{q}'$ as well as the wave vectors $\mathbf{k}_{23},\mathbf{k}'_{23}$ of the scattered neutrons follow from the scattering surface. In general the flight-times T and T' of the neutrons for the two scattering processes differ from each other. The locus of end-points of wave vector pairs $\mathbf{k}'_{12},\mathbf{k}'_{23}$ giving identical flight-times is a surface which will be called the *focusing surface* of the monochromator ellipsoid. From the equality $T=T'$ one obtains the appropriate wave-numbers k'_{23} as

$$\tilde{k}_{23}=L_{23}\left[\frac{L_{12}}{k_{12}}+\frac{L_{23}}{k_{23}}-\frac{L_{12}}{k'_{12}}-\frac{\hbar}{m}\Delta T'\right]^{-1}. \quad (2\cdot3)$$

$\Delta T'$ is the shift of the mean emission time of neutrons with wave-vector $\mathbf{k}'_{12}$ relative to those with wave-vector $\mathbf{k}_{12}$. It is independent of the vertical divergence angle δ_{12} and can be calculated from equation (2·2) by searching the maximum of g_{12} for fixed values of k'_{12} and γ_{12}:

$$\Delta T'=\frac{\left(1-\frac{k'_{12}}{k_{12}}\right)\mathrm{tg}\,\theta_1-\gamma_{12}}{2\pi v}. \quad (2\cdot4)$$

Wave-vector pairs lying outside the focusing surface give rise to a time-of-flight difference which is given by

$$\delta_1 T=\frac{mL_{23}}{\hbar}\left(\frac{1}{k'_{23}}-\frac{1}{\tilde{k}_{23}}\right), \quad (2\cdot5)$$

where k'_{23} results from the scattering surface and $\tilde{k}_{23}$ is defined by equation (2·3). The 50% probability spread is obtained by considering incoming neutron wave-vectors $\mathbf{k}'_{12}$ with $g_{12}=0{\cdot}5$.

It can be seen intuitively from Fig. 3 that the mean value of $\delta_1 T$ will be a minimum when the focusing surface coincides with a vertical plane containing the principal axis of the monochromator ellipsoid. In order to achieve this the following experimental parameters can be varied: the wave-vector $\mathbf{k}_{12}$ and the Bragg angle θ_1 of the incoming neutron beam, the reciprocal-lattice vector $2\pi\tau$ determining the momentum transfer $\hbar\mathbf{Q}=\hbar(2\pi\tau+\mathbf{q})$, the orientation of $\mathbf{k}_{12}$ and $\mathbf{q}$ with respect to $2\pi\tau$, and the length of the neutron flight-path L_{23}; moreover, in many cases one can carry out the scattering process either with energy loss or with energy gain of the neutrons, thus duplicating the range of variation. The parameters α_{01}, β_{01}, ξ_1, η_1, α_{12}, β_{12} have only little influence on the orientation of the focusing surface. By reducing these parameters the monochromator ellipse will become smaller as shown in Fig. 2, thus reducing the time-of-flight spread $\delta_1 T$. A variation of the spin velocity v of the rotating crystal and of the flight-path L_{12} is not at all commendable, because these are the appropriate parameters to eliminate the time-of-flight uncertainty from the Doppler effect, as demonstrated in the following subsection. However, to realize efficient focusing effects, the sense of monochromator rotation has to be chosen so that the reflecting planes reach the Bragg position with decreasing angle. Thus the slower neutrons get a start advantage relative to the faster ones as can be seen from equation (2·4).

2·2. *Doppler effect*

In contrast with the Bragg reflexion from the stationary monochromator, the neutrons scattered elastically from the rotating monochromator receive a supplementary momentum $2m\mathbf{v}$, where $\mathbf{v}$ is the velocity component of a small element of the monochromator perpendicular to the reflecting planes. Therefore Bragg's law (2·1) has to be modified in such a way that $\mathbf{k}_{01}$ and $\mathbf{k}_{12}$ are no longer equal in length, whereas the momentum transfer and the angle of deflection as usual have the values $2\pi\hbar\tau$ and $2\theta_1$ respectively. The appropriate reciprocal space diagram is shown in Fig. 4, which illustrates both the deviation of k^B_{12} from the mean wave-number k^A_{12} associated with the stationary reflexion and the shift ΔT^B of the mean emission time of the neutron burst owing to the deflection of $\mathbf{k}^B_{01}$ relative to $\mathbf{k}^A_{01}$ by the angle ε. These effects were investigated in detail by Meister (1967). He showed that the above mentioned differences in wave-number and emission time depend linearly on the coordinate y indicated in Fig. 5. In a first approximation the calculation yields

$$k^B_{12}-k^A_{12}=\frac{2\pi v m y\sin\theta_1}{\hbar}, \quad (2\cdot6)$$

$$\Delta T^B=\frac{my\cos\theta_1}{\hbar k^A_{12}}. \quad (2\cdot7)$$

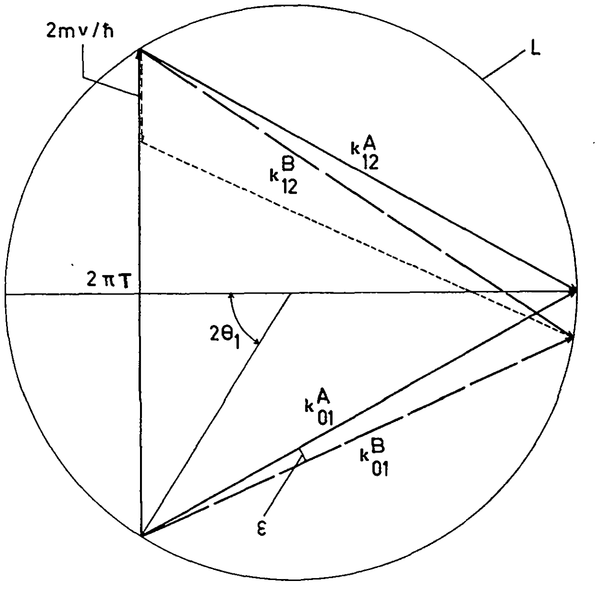

Fig. 4. Schematic sketch of the Doppler effect in reciprocal space. The two pairs of wave vectors $\mathbf{k}_{01}{}^A$, $\mathbf{k}_{12}{}^A$ and $\mathbf{k}^B{}_{01}$, $\mathbf{k}_{12}{}^B$ are associated with elastic scattering from the monochromator crystal at rest and in rotation respectively. The circle L is the locus of end-points of the incoming and scattered neutron wave vectors including the scattering angle $2\theta_1$.

The idea of optimum focusing then consists in trying to equalize the neutron flight-times T_A and T_B for different reflecting planes A and B of the monochromator as shown in Fig. 5:

$$T_A = \frac{mL_{12}}{\hbar k_{12}^A} + \frac{mL_{23}}{\hbar k_{23}^A} = \frac{m\left(L_{12} + \dfrac{y}{\cos\theta_1}\right)}{\hbar k_{12}^B} + \frac{mL_{23}}{\hbar k_{23}^B} + \Delta T^B = T_B\,. \qquad (2{\cdot}8)$$

k_{23}^B results from the scattering surface. It should be noted that equation (2·8) eliminates the time-of-flight uncertainty due to the finite width of the monochromator crystal. Combining equations (2·6), (2·7), and (2·8) yields the focusing condition

$$\nu = \frac{\hbar k_{12}^A}{2\pi m \sin\theta_1 (L_{12}\cos\theta_1 + y)} \times \left[1 + \cos^2\theta_1 \frac{L_{23} k_{12}^A (k_{23}^B - k_{23}^A)\cos\theta_1}{y (k_{23}^A)^2}\right], \qquad (2{\cdot}9)$$

provided that $|k_{12}^B - k_{12}^A| \ll k_{12}^A$ and $|k_{23}^B - k_{23}^A| \ll k_{23}^A$. If the curvature of the dispersion surface is small around the point $(\mathbf{Q},\omega)$, equation (2·9) will be independent of y in a first approximation.

There remains a certain time-of-flight spread $\delta_2 T$, when the dispersion surface has any appreciable curvature or when the condition (2·9) cannot be fulfilled on account of instrumental restrictions. The resulting time-of-flight spread $\delta_2 T$ is then given by equation (2·5), where k'_{23} follows from the phonon scattering surface and $\tilde{k}_{23}$ is equal to k_{23}^B derived from equation (2·8). To obtain the 50% probability spread y has to take the values $r\sqrt{3}/2$ and $r\sqrt{2}/2$ for monochromator crystals of cylindrical and spherical shape respectively, where r denotes the crystal radius.

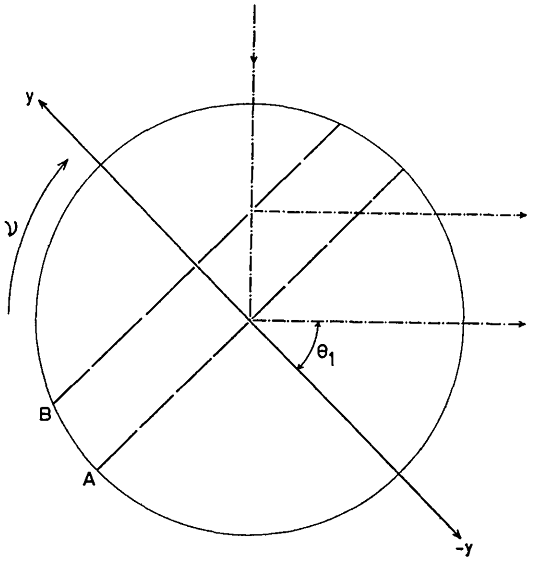

Fig. 5. Schematic sketch of the rotating monochromator. Reflecting planes are parallel to the y axis which is perpendicular to the bisector of the angle between the incoming and scattered neutrons. Planes perpendicular to y (*e.g.* the planes A and B) scatter neutrons with equal velocities.

3. Irremovable time-of-flight uncertainties

3·1. *Mosaic spread of the sample*

The finite mosaic spreads ξ_2 and η_2 of the sample smear out the wave-vector $\mathbf{q}$ of the observed phonon as shown in Fig. 6(*a*) for the horizontal component. The contribution $\delta_3 T$ to the time-of-flight spread is calculated using equation (2·5), where k'_{23} is derived from the phonon scattering surface and $\tilde{k}_{23}$ is equal to k_{23}.

3·2. *Collimation between the sample and the detector*

A similar effect arises from the finite collimations α_{23} and β_{23}. This is shown in the reciprocal-lattice diagram of Fig. 6(*b*) for the horizontal plane. The corresponding time-of-flight spread $\delta_4 T$ is likewise derived from equa-

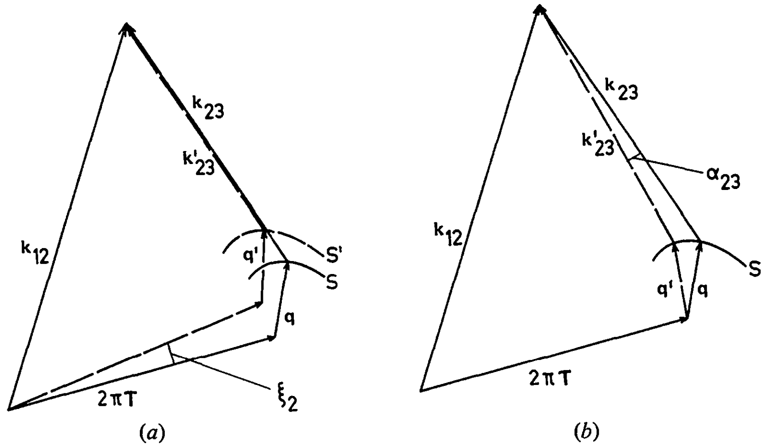

(*a*) (*b*)

Fig. 6. Schematic representation of the contributions to the irremovable time-of-flight uncertainty arising (*a*) from the finite mosaic spread ξ_2 of the sample, (*b*) from the finite collimation α_{23}.

tion (2·5), where k'_{23} results from the phonon scattering surface and $\tilde{k}_{23}$ equals k_{23}.

3·3. *Sample thickness*

The sample is considered to be placed within a sector bounded by two planes perpendicular to the incoming and outgoing neutron beam as shown in Fig. 7. Within this sector curves of constant flight-times are given by a set of straight lines

$$x\left(\frac{1}{k_{12}}-\frac{\cos\psi}{k_{23}}\right)+y\,\frac{\sin\psi}{k_{23}}=\text{constant}\,, \qquad (3\cdot1)$$

where the y axis of the rectangular coordinate system is perpendicular to the incoming neutron beam. A simple integration procedure then furnishes the time-of-flight spread, provided the whole sample is uniformly irradiated by the neutrons. Using (3·1) one obtains

$$\delta_5T=\frac{mW_S\sqrt{k_{12}^2-2k_{12}k_{23}\cos\psi+k_{23}^2}}{\hbar k_{12}k_{23}}\,. \qquad (3\cdot2)$$

W_S is a characteristic length depending on the shape of the sample. To obtain the 50% probability spread W_S has to be equal to $D\sin\varphi$ for a plate, $r\sqrt{3}$ for a cylinder, and $r\sqrt{2}$ for a sphere, where r denotes the radius of the cylinder and the sphere, and D the width of the plate, whose inclination angle relative to the set of straight lines (3·1) is given by φ. Consequently δ_5T vanishes for thin plates positioned in such a manner that $\varphi=0$.

3·4. *Detector thickness*

As in all time-of-flight experiments, the thickness of the counters introduces an uncertainty into the flight-path and thus gives rise to an irremovable time-of-flight spread whose half-width is given by

$$\delta_6T=\frac{mW_d}{\hbar k_{23}}\,. \qquad (3\cdot3)$$

W_d is equal to the half-width of the response probability $P(x)$ depending on shape and size of the detector, on the absorption properties and pressure of the filling gas, and on the wave-number k_{23}. It follows from simple geometrical considerations that for a cylindrical detector the response probability is given by

$$P(x)=C\,\frac{1}{r}\exp\{-\mu(x-r)\}$$
$$\times\int_0^{\sqrt{x(2r-x)}}\exp\{-\mu\sqrt{r^2-y^2}\}\mathrm{d}y\,, \qquad (3\cdot4)$$

using an exponential absorption law. In this formula C denotes the normalization constant, r the radius of the detector, and μ the linear absorption coefficient. A general discussion of $P(x)$ is not possible because the integral cannot be solved analytically. However, the first terms of equation (3·4) suggest a minimal half-width W_d for small radii r and large absorption coefficients μ. This is verified in Fig. 8, presenting W_d as a function of radius, gas pressure, and neutron energy for a ^{3}He detector.

Experimental results

The calculation of the effective resolution function for phonon scattering $R_\sigma(T)$ requires a precise knowledge of the instrumental parameters α_{01}, β_{01}, α_{12}, β_{12}, α_{23}, β_{23}, ξ_1, η_1, ξ_2, η_2, y, W_s, W_d, the values of which should preferably be determined experimentally except for those of the collimations α and β which can be calculated exactly from the collimator dimensions. Such calibration experiments are carried out by observing the coherent elastic scattering from the sample at various speeds of rotation v, Bragg angles θ_1 and θ_2, neutron wave-numbers k_{12}, and flight-paths L_{12} and L_{23}. The set of resolution functions thus obtained for zero energy transfer may then be used to adapt the instrumental parameters with the aid of a variational procedure. This will be discussed in detail in Appendix *B*.

The formulae described in the foregoing sections are now examined by means of experimental phonon peaks obtained with a lead single crystal (Furrer & Hälg, 1970). The sample was a cylinder 4 cm in diameter and 6 cm in height. The mosaic spreads ξ_2 and η_2 amounted to about 25′.

4·1. *Gaussian approximation*

Whenever the individual time-of-flight uncertainties δ_iT derived in §§ 2 and 3 can be approximated by Gaussian functions, it is useful to describe $R_\sigma(T)$ by its half-width

$$\Gamma_r=\sqrt{\sum_{i=1}^{6}(\delta_iT)^2}\,, \qquad (4\cdot1)$$

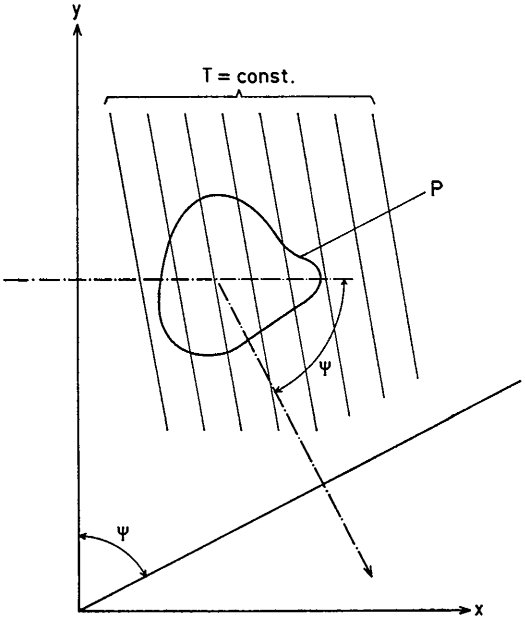

Fig. 7. Schematic sketch explaining the irremovable time-of-flight spread due to the thickness of the sample *P*. The set of straight lines correspond to the curves of different flight-times being constant within the sector determined by the scattering angle ψ.

where the contributions $\delta_i T$ are derived by considering the 50% probability spread. To test rigorously the calculated half-widths Γ_r, the comparison is made at 5 K, where the width $\Gamma_\sigma(\mathbf{q})$ of the phonon line may be replaced in a first approximation by a δ function. Thus the observed peaks are nearly equal to the effective resolution functions for phonon scattering. Fig. 9 shows a series of experimental time-of-flight spectra carried out for various degrees of focusing together with the corresponding wave-vector constellations in reciprocal space. The observed and calculated widths are given in Table 2. In general the over-all agreement between observed and calculated widths is seen to be satisfactory. However, in almost all cases, the observed widths turn out to be slightly larger than the predicted ones. These deviations are attributable to the presence of finite phonon life-times.

Table 2. *Observed and calculated widths of phonon peaks shown in Fig.* 9

	A	*B*	*C*	*D*	*E*
ω[THz]	7·1	7·2	5·4	12·3	8·7
$\delta_1 T$[μsec]	46·8	35·6	57·8	54·6	36·0
$\delta_2 T$[μsec]	14·6	17·5	17·9	16·8	20·8
$\delta_3 T$[μsec]	5·2	0·8	12·9	0·5	3·7
$\delta_4 T$[μsec]	9·4	5·8	10·0	7·8	7·8
$\delta_5 T$[μsec]	48·6	49·6	31·4	21·6	22·7
$\delta_6 T$[μsec]	11·3	11·2	11·8	14·2	14·5
Γ_r[μsec]	70·8	64·7	71·1	63·2	50·3
Γ_{exp}[μsec]	75·4 ± 6·7	70·4 ± 7·2	68·4 ± 6·7	62·7 ± 6·1	52·4 ± 3·9

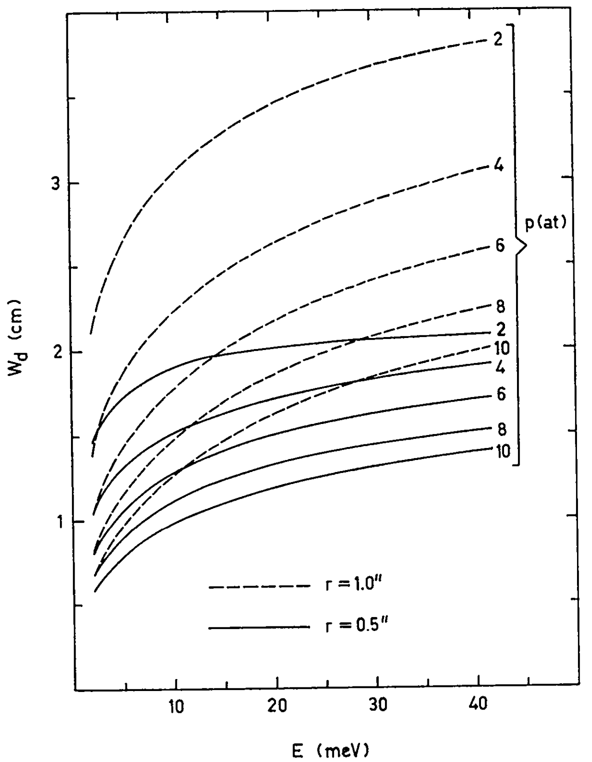

Fig. 8. Half-widths W_d of the response probability $P(x)$ as a function of gas pressure p, neutron energy E, and radius r for a ^{3}He detector.

4·2. *Non-Gaussian case*

More precise results will be obtained by an exact calculation of the shape of the resolution function. This is indispensable whenever the individual contributions to $R_\sigma(T)$ may no longer be approximated by Gaussian functions. It can be shown that $R_\sigma(T)$ becomes asymmetric in shape when the dispersion surface possesses an appreciable curvature or exhibits anomalies around the point $(\mathbf{Q}, \omega)$, where the spectrometer has been set to realize the scattering process.

The result of such a calculation is illustrated in Fig. 10 for a longitudinal phonon of wave-number 0·77 Å^{-1} propagating along the Λ direction at 290K. In case 1 $R_\sigma(T)$ has been determined by using the Gaussian approximation which results in a symmetrical function. In case 2, however, $R_\sigma(T)$ has been calculated on the basis of a sampling procedure, thus taking into account the asymmetries mentioned above. To get the phonon profile $\sigma(T)$ the experimental spectrum $I(T)$ was deconvoluted according to equation (1·6) with the aid of the computer program *CSUP* developed by Dotti (1967). As a result the phonon lines $\sigma(T)$ obtained in cases 1 and 2 reveal marked differences not only in the shape but also in the mean position and width. Thus it is proved that systematic errors in the observed phonon dispersion may arise from approximations generally used to evaluate the effective resolution functions for phonon scattering.

5. Summary

The experimental spectra observed using a spectrometer are distorted by the finite instrumental resolution. To obtain precise experimental data the resolution function has to be known exactly. Moreover focusing conditions should be such as to minimize the width of the observed peaks. These postulates have been treated analytically for a rotating crystal time-of-flight spectrometer applied to the measurement of phonon dispersions by introducing the concept of removable and irremovable time-of-flight spreads. To derive the unknown scattering cross section $\sigma(\mathbf{Q}, \omega)$ it has been assumed that the resolution function does not change over a small frequency range $d\omega$ given by the finite width of the dispersion surface, while $\mathbf{Q}$ is kept constant. This is valid only if the shape of the phonon line is symmetrical and if $d\omega \ll \omega$. No approximations are made concerning the phonon dispersion surface in contrast to earlier investigations (Collins, 1963; Peckham *et al.*, 1967; Cooper & Nathans, 1967; Stedman, 1968) where the dispersion surface is generally considered to be plane. Experiments carried out on lead (Furrer & Hälg, 1970) on the basis of the present theory yielded an experimental error of 1–2% for the phonon frequencies and 20–30% for the phonon widths at 290K.

The integrated intensity of a neutron group is calculated from equations (1·6) as

$$I_{\text{tot}}=\int I(T)\mathrm{d}T\,, \tag{5·1}$$

but this formula is only applicable to the limitations mentioned above. In addition the restriction $\mathrm{d}Q \ll Q$ must be satisfied because of the variation of the structure factor. This means that the present theory is a good approach to determine resolution function shapes, but the calculation of intensities will only give reliable results for small momentum and frequency spreads.

It is worth while mentioning here that the procedure described in this paper may be applied to all kinds of excitation measurements as well. Moreover, it can easily by adapted either to a spectrometer at a pulsed neutron source or to a randomly pulsed experiment.

The Fortran program *TOFFOC* (Furrer, 1971) evaluating resolution functions and focusing conditions is available from the author on request.

I wish to acknowledge the numerous and stimulating discussions with my colleagues Dr W. Bührer and Dr P. Fischer. In particular I am grateful to Professor W. Hälg for his continuous support of this research.

APPENDIX *A*

Since the wave-number distribution $g_0(\gamma,\delta,k)$ of the in-pile neutrons is generally isotropic, the angular variables γ and δ may be omitted. By defining the horizontal and vertical divergence angles with respect to the optimum directions to be γ_{01}, γ_1, γ_{12}, and δ_{01}, δ_1, δ_{12} respectively, the wave-number distribution of the neutrons emitted from the monochromator is given by

$$\begin{aligned} g(k'_{12},\gamma_{01},\gamma_1,\gamma_{12},\delta_{01},\delta_1,\delta_{12},t)&=g_0(k'_{12})p_1(k'_{12}) \\ \times\exp\Bigg\{&-\frac{4\ln2}{\alpha_{01}^2}\gamma_{01}^2-\frac{4\ln2}{\xi_1^2}\left[\gamma_1-2\pi\left(vt-\frac{u}{w}\right)\right]^2 \\ &-\frac{4\ln2}{\alpha_{12}^2}\gamma_{12}^2-\frac{4\ln2}{\beta_{10}^2}\delta_{01}^2-\frac{4\ln2}{\eta_1^2}\delta_1^2-\frac{4\ln2}{\beta_{12}^2}\delta_{12}^2\Bigg\}\,. \end{aligned} \tag{A1}$$

From the reflexion law it is easy to derive the equalities

$$\gamma_{01}+2\gamma_1=\gamma_{12}\,, \tag{A2}$$

$$\delta_{01}+2\delta_1\sin\theta_1=\delta_{12}\,, \tag{A3}$$

where the divergence angles take the positive sign when the angle of Bragg reflexion is increased. A second condition for the horizontal divergence angles results from the derivative of equation (2·1):

$$\gamma_{01}+\gamma_1=\left(1-\frac{k'_{12}}{k_{12}}\right)\operatorname{tg}\theta_1\,\cdot \tag{A4}$$

The final form of g_{12} is then obtained by combining

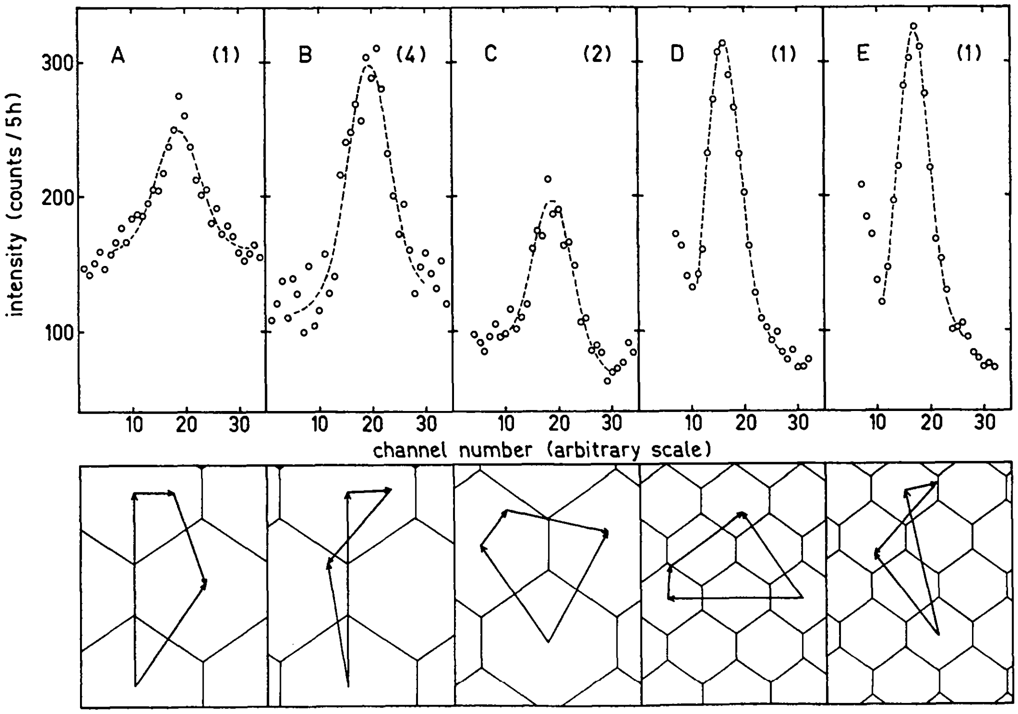

Fig. 9. Observed phonon peaks from time-of-flight spectra for lead at 5 K, together with the corresponding experimental constellations in a (110) plane. The dotted lines denote Gaussian functions adapted to the experimental profiles. The numbers in brackets are the factors by which the intensity has been multiplied. The channel width has a value of 8 μsec, corresponding to mean frequency widths of 0·09 THz in cases *A* and *B*, 0·11 THz in case *C*, 0·27 THz in case *D*, and 0·31 THz in case *E*.

equations ($A1$), ($A2$), ($A3$), and ($A4$) and integrating the vertical terms over δ_{01} to eliminate γ_{01}, γ_1, δ_{01} and δ_1 as shown in equation (2·2a).

APPENDIX *B*

The instrumental resolution functions $R(T)$ experimentally obtained for zero energy transfer are well approximated by Gaussian functions. The corresponding half-widths are equal to

$$\Gamma_r = \sqrt{(\delta_a T)^2 + (\delta_b T)^2 + (\delta_c T)^2 + (\delta_d T)^2}\,. \qquad (B1)$$

The individual contributions are defined in the following paragraphs.

$\delta_a T$ results from the wave-number distribution of the neutrons emitted by the sample. Paying attention to the equalities $k_{12}=k_{23}$ and $k'_{12}=k'_{23}$ one obtains

$$g_{23}(k'_{23}, \gamma_{12}, \gamma_2, \gamma_{23}, \delta_{12}, \delta_2, \delta_{23}, t) = g_{12}(k'_{23}, \gamma_{12}, \delta_{12}, t) p_2(k'_{23})$$

$$\times\ \exp\left\{-\frac{4\ln 2}{\xi_2^2}\gamma_2^2 - \frac{4\ln 2}{\alpha_{23}^2}\gamma_{23}^2 - \frac{4\ln 2}{\eta_2^2}\delta_2^2 - \frac{4\ln 2}{\beta_{23}^2}\delta_{23}^2\right\}, \qquad (B2)$$

where g_{12} is defined by equation (2·2a) and p_2 denotes the sample reflectivity. By applying equations ($A2$), ($A3$), and ($A4$) to the elastic reflexion from the sample and integrating the vertical terms over δ_{12} the wave-number distribution g_{23} can be written in the form

$$\begin{aligned} g_{23}(k'_{23}, \gamma_{23}, \delta_{23}, t) &= g_0(k'_{23}) p_1(k'_{23}) p_2(k'_{23}) \frac{\pi}{4ab\ln 2} \\ &\times\ \exp\left\{-\frac{4\ln 2}{\alpha_{01}^2}\left[\gamma_{23} + 2\left(1-\frac{k'_{23}}{k_{23}}\right)\left(\operatorname{tg}\theta_1 - \operatorname{tg}\theta_2\right)\right]^2\right. \\ &- \frac{4\ln 2}{\xi_1^2}\left[\gamma_{23} + \left(1-\frac{k'_{23}}{k_{23}}\right)(\operatorname{tg}\theta_1 - 2\operatorname{tg}\theta_2)\right. \\ &\left. + 2\pi\left(vt - \frac{u}{w}\right)\right]^2 - \frac{4\ln 2}{\alpha_{12}^2}\left[\gamma_{23} - 2\left(1-\frac{k'_{23}}{k_{23}}\right)\operatorname{tg}\theta_2\right]^2 \\ &- \frac{4\ln 2}{\xi_2^2}\left[\gamma_{23} - \left(1-\frac{k'_{23}}{k_{23}}\right)\operatorname{tg}\theta_2\right]^2 - \frac{4\ln 2}{\alpha_{23}^2}\gamma_{23}^2 \\ &\left. - \frac{4\ln 2}{4\eta_2^2\sin^2\theta_2}\left(1 - \frac{1}{4b^2\eta_2^2\sin^2\theta_2}\right)\delta_{23}^2 - \frac{4\ln 2}{\beta_{23}^2}\delta_{23}^2\right\} \end{aligned} \qquad (B3a)$$

with

$$b = \sqrt{\frac{1}{\beta_{01}^2 + 4\eta_1^2\sin^2\theta_1} + \frac{1}{\beta_{12}^2} + \frac{1}{4\eta_2^2\sin^2\theta_2}}\,. \qquad (B3b)$$

The corresponding half-width is then given by

$$\delta_a T = \frac{m(L_{12}+L_{23})}{\hbar}\left(\frac{1}{(k'_{23})_{\min}} - \frac{1}{(k'_{23})_{\max}}\right), \qquad (B4)$$

where $(k'_{23})_{\min}$ and $(k'_{23})_{\max}$ result from equation ($B3a$) by considering the minimal and maximal values k'_{23} of the 50% probability distribution.

The Doppler effect gives rise to the contribution $\delta_b T$ which can be calculated from equations (2·6), (2·7), and (2·8) as

$$\delta_b T = \frac{2my}{\hbar k_{23}^4}\left[2\pi v m \sin\theta_1\left(L_{12} + L_{23} + \frac{y}{\cos\theta_1}\right) - \frac{1+\cos^2\theta_1}{\cos\theta_1}\right]. \qquad (B5)$$

The time-of-flight spreads $\delta_c T$ and $\delta_d T$ due to the thickness of both the sample and the detector will be

$$\delta_c T = \frac{mW_s\sqrt{2(1-\cos\psi)}}{\hbar k_{23}}, \qquad (B6)$$

$$\delta_d T = \frac{mW_d}{\hbar k_{23}} \qquad (B7)$$

according to equations (3·2) and (3·3).

Using a set of resolution functions obtained at various experimental conditions the instrumental parameters ξ_1, η_1, ξ_2, η_2, y, W_s and W_d can be determined on the basis of equation ($B1$) with the aid of a variational procedure.

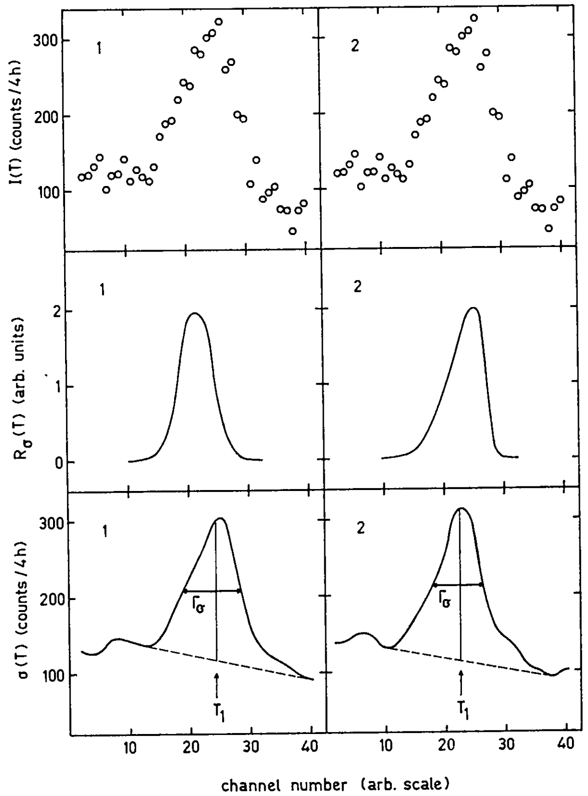

Fig. 10. Representation of the unfolding procedure for a time-of-flight spectrum $I(T)$ with 8μsec channel width. In case 1 the effective resolution function for phonon scattering has been determined using the Gaussian approximation. In case 2 the calculation of $R_\sigma(T)$ has been based on a sampling procedure. The resulting phonon lines $\sigma(T)$ reveal the following properties (the values in brackets denote the corresponding phonon frequencies and widths). Case 1: T_1= channel number 24·2 (12·90 THz); Γ_σ=9·7 channels (0·70 THz). Case 2: T_1=channel number 22·0 (12·74 THz); Γ_σ= 8·3 channels (0·60 THz).

References

BROCKHOUSE, B. N. (1961). *Inelastic Scattering of Neutrons in Solids and Liquids*, p. 113. Vienna: IAEA.

CARVALHO, F., EHRET, G. & GLÄSER, W. (1967). *Nucl. Instrum. Methods*, **49**, 197.

COLLINS, M. F. (1963). *Brit. J. Appl. Phys.* **14**, 805.

COOPER, M. J. & NATHANS, R. (1967). *Acta Cryst.* **23**, 357.

DOTTI, D. (1967). *Nucl. Instrum. Methods*, **54**, 125.

FURRER, A. (1971). Report AF-SSP-45, Wuerenlingen.

FURRER, A. & HÄLG, W. (1970). *Phys. stat. sol.* **42**, 821.

KOMURA, S. & COOPER, M. J. (1970). *Japan. J. Appl. Phys.* **9**, 866.

MEISTER, H. (1967). *Nukleonik*, **10**, 97.

NIELSEN, M. & BJERRUM MØLLER, H. (1969). *Acta Cryst.* A**25**, 547.

PECKHAM, G. E., SAUNDERSON, D. H. & SHARP, R. I. (1967). *Brit. J. Appl. Phys.* **18**, 473.

STEDMAN, R. (1968). *Rev. Sci. Instrum.* **39**, 878.

Acta Cryst. (1971). A**27**, 470

Classifications of Magnetic Structures

BY W. OPECHOWSKI AND TOMMY DREYFUS*

Department of Physics, University of British Columbia, Vancouver, Canada

(*Received* 17 *August* 1970)

Two different classification schemes have been used for concise characterization of magnetic structures: one (called here $C1'$) making use of magnetic groups, and another, more recent (called here $C2$), in which representations of space groups play an essential part. While the mathematical principles of $C1'$ have already been formulated in all their generality, this is not so in the case of $C2$ (although many magnetic structures have been discussed from the point of view of $C2$). In this paper the principles of $C2$ are formulated in a mathematically general way, a link between $C1'$ and $C2$ is established, and a few illustrative examples of magnetic structures are discussed. It turns out that $C1'$ and $C2$ are equivalent in a precise mathematical sense, provided cyclic boundary conditions are imposed on the crystal; each magnetic structure has then its appropriate label in both classifications. If, however, one is not willing to impose such conditions, $C2$ may in some cases (as for example helical structures) meet with mathematical difficulties while $C1'$ never does. Claims made by Bertaut (*Acta Cryst.* (1968). A**24**, 217) that $C2$ is 'more general' than $C1'$ are thus unjustified.

1. Introduction

The phrase *magnetic structure* has many connotations in solid state physics. When discussing the problem of classification of magnetic structures we will take this phrase to mean nothing else than an axial vector function that changes sign under time inversion and is defined on a set of points ('atoms') which form an ideal crystal, or any other atom arrangement. To stress that only this particular meaning is to be attached to the term magnetic structure, we shall most of the time use instead of it the term *spin arrangement*, and shall call, as is customary, the vectors *spin vectors*.

An assignment of a label to each spin arrangement is called here a *classification* of all spin arrangements if

(*a*) the label characterizes the spin arrangement completely; that is, the label allows one, from the information contained in it, to construct the whole spin arrangement;

(*b*) one obtains a list of all spin arrangements by letting the symbols occurring in the label vary over a specified class of symbols.

The problem of classification of all spin arrangements is thus a special case of the general mathematical problem of classification of all (scalar or vector or tensor *etc.*) functions defined on a discrete set of points.

If one applies an element of the space group F of a crystal to a scalar or vector function defined on it, then the function will either remain unchanged or be transformed into another function defined on the came crystal. This trivial remark makes it clear that there are two obvious ways of classifying all such functions: (1) by assigning to each function the subgroup H of F consisting of all those elements of F which leave the function unchanged (we shall call this *classification* $C1$); (2) by assigning to each function all those distinct functions which arise from it by applying the elements of F; this is equivalent to assigning a permutation representation of F according to which those distinct functions transform, or, as it will turn out, an appropriate component of such representation (we shall call this *classification* $C2$).

If a function changes sign under time inversion, as spin arrangements do, classification $C1$ can be use-

---

[*] Present address: Institut de physique théorique, Université, Genève, Switzerland.